ACS OMEGA

http://pubs.acs.org/journal/acsodf

Article

Thermoelectric Properties of PEDOT:PSS Containing Connected Copper Selenide Nanowires Synthesized by the Photoreduction Method

Shunya Sakane, Shunichiro Miwa, Tatsuki Miura, Kazuki Munakata, Takafumi Ishibe, Yoshiaki Nakamura, and Hideki Tanaka*

Cite This: *ACS Omega* 2022, 7, 32101−32107

Read Online

ACCESS | Metrics & More | Article Recommendations | Supporting Information

ABSTRACT: Organic materials have attracted attention for thermoelectric materials reusing low-temperature waste heat. For the thermoelectric performance enhancement of organic materials, the introduction of inorganic nanowires is effective due to the percolation effect. In this study, we synthesized Cu_2Se NWs by the photoreduction method and prepared poly(3,4-ethylenedioxythiophene):poly (styrene sulfonate) (PEDOT:PSS) thin films containing Cu_2Se NWs by spin-coating PEDOT:PSS and Cu_2Se NWs alternatively. The composite films exhibited a drastic increase in electrical conductivity at more than 40 wt % Cu_2Se, and the Cu_2Se amount threshold was in good agreement with surface structures as observed by a scanning electron microscope. This indicates that the percolation effect of connected Cu_2Se NWs brought high electrical conductivity. As a result, the composite thin films exhibited a higher power factor than the PEDOT:PSS film. This power factor enhancement by the percolation effect would be expected to contribute to the development of thermoelectric performance enhancement for organic materials.

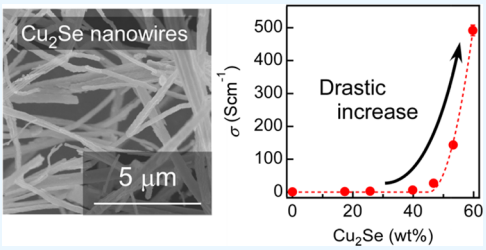

INTRODUCTION

Thermoelectric conversion is expected as one of the energy harvesting techniques. Thermoelectric conversion efficiency is represented by ZT $(=S^2\sigma T/\kappa)$, where S is the Seebeck coefficient, σ is the electrical conductivity, κ is the thermal conductivity, and T is the absolute temperature.[1,2] For high thermoelectric performance, high S and σ and low κ are required. While the trade-off relationship of the above three parameters has been bottlenecked for improving thermoelectric performance, to remove the bottleneck, nanostructuring is an effective approach.[3] The nanostructure interface can bring phonon scattering, leading to κ reduction,[4−15] which can control thermal flow[16−19] and affect the carrier scattering mechanism, leading to S enhancement, such as the energy filtering effect.[20−22]

It is effective to introduce inorganic nanostructures for improving the thermoelectric performance of organic materials, such as poly(3,4-ethylenedioxythiophene):poly (styrene sulfonate) (PEDOT:PSS), which have attracted attention for low-temperature waste heat due to their low cost, eco-friendliness, and flexibility.[23−31] Especially, the introduction of one-dimensional nanostructures, such as carbon nanotubes or Te nanowires, effectively enhanced the thermoelectric power factor $(S^2\sigma)$ of PEDOT:PSS due to the formation of a conductive path.[32,33]

Cu_2Se is also a promising candidate for inorganic nanostructures because it is low cost, has abundant elements, and exhibits high thermoelectric performance depending on its crystal structure. Bulk α-Cu_2Se has recently been found to exhibit a high average ZT of 0.68 near RT (RT-390 K).[34] It is also worth noting that this α-phase tends to be contaminated with a small amount of the β-phase, resulting in lower ZT due to higher carrier concentration than the optimal value.[35] Therefore, it is expected to enhance the thermoelectric performance of PEDOT:PSS by the introduction of Cu_2Se nanowires (NWs). Although Cu_2Se NWs have been synthesized by various methods, it is difficult to maintain only the α-phase even at RT when Cu_2Se were nanostructured.[36−38] This is because increasing Cu vacancies distorted the structures of the α-phase until rearrangement of the β-phase is energetically favorable due to the larger contribution of the surface energy to the total energy of formation than that of bulk.[39]

In this study, we synthesized α-Cu_2Se NWs by the photoreduction method and evaluated the thermoelectric properties of PEDOT:PSS/Cu_2Se NW composite thin films with various amounts of Cu_2Se NWs. In previous reports, we demonstrated the synthesis of size-controlled Cu nanoparticles

Received: May 28, 2022
Accepted: August 25, 2022
Published: September 5, 2022

by the photoreduction method,[40−43] where the slow reaction can control the morphology of copper nanoparticles.[42] We applied the above method to the synthesis of α-Cu_2Se NWs. The slow reaction can be expected to control the Cu vacancies, leading to the synthesis of Cu_2Se NWs. As a result, the composite thin films exhibited a higher thermoelectric power factor ($S^2\sigma$) than pristine PEDOT:PSS thin films due to the percolation effect of NWs. This study would be expected to contribute to the development of thermoelectric performance enhancement for organic materials.

EXPERIMENTAL SECTION

Synthesis of Cu_2Se NWs. Se NWs were synthesized by the following method.[44] SeO_2 (25 mg, FUJIFILM Wako Pure Chemical Corporation) and β-cyclodextrin (50 mg, FUJIFILM Wako Pure Chemical Corporation) were dissolved in 10 mL of Milli-Q water and stirred with ultrasonication for 10 min. The solution was slowly added to an L-ascorbic acid solution prepared with L-ascorbic acid (0.2000 g, Wako Pure Chemical Corporation) and Milli-Q water (10 mL) and stirred for 4 h. The mixed solution was centrifuged and the resulting precipitates were washed with EtOH and Milli-Q water several times alternately. The precipitates were redispersed in EtOH and stirred for 4 h, forming Se NWs as precipitates.

The Se NWs (2.0 mg) were dispersed in a copper acetate solution prepared by dissolving 50.6 μmol of copper acetate in an aqueous solution containing 1 mL of ethanol. The total volume of the dispersion thus obtained was adjusted to 10 mL by Milli-Q water. The adjusted dispersion was irradiated by UV light (Hamamatsu Photonics: L9588-01A) for 2 h with stirring, and Cu_2Se NWs were obtained as precipitates.

Preparation of PEDOT:PSS Thin Films Containing Cu_2Se NWs. The fabrication process of PEDOT:PSS thin films containing Cu_2Se NWs is schematically shown in Figure 1. First, a pH-neutral PEDOT:PSS solution (100 μL, N-1005, Orgacon) was dropped, spin-coated (1500 rpm, 45 s), and annealed (80 °C, 20 min) on a glass substrate of 10 mm × 10 mm, which was cleaned and hydrophilized by piranha solution (a mixture of H_2SO_4 and H_2O_2). The PEDOT:PSS layer was formed in this way. Second, Cu_2Se NWs (0.18 mg) dispersed in ethanol (30 μL) were deposited, spin-coated, and annealed (80 °C, 5 min) on the substrate. The NW layer was accumulated n times. Finally, the PEDOT:PSS solution (100 μL) was dropped, spin-coated, and annealed (80 °C, 20 min) on the substrate again. The thin film thus obtained is abbreviated as NW-n in this paper. NW-0 (without Cu_2Se NWs) was prepared by spin-coating PEDOT:PSS once. The reference thin film was also prepared using EtOH solution without Cu_2Se NWs instead of the EtOH dispersion of Cu_2Se NWs ("NW-0-EtOH-8"). The crystal structures of NWs and thin films were characterized by X-ray diffraction (XRD) with an X-ray diffractometer (Rigaku, Smartlab) and scanning electron microscopy (SEM)−energy-dispersive X-ray spectroscopy (EDX) with a field emission SEM (Hitachi High-Technologies, S-5500), respectively.

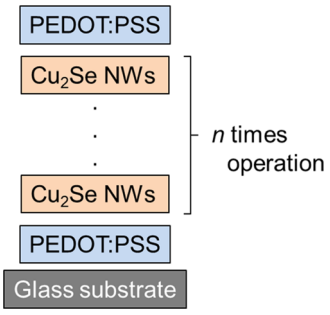

Figure 1. Fabrication process of PEDOT:PSS thin films containing Cu_2Se NWs on a glass substrate.

Evaluation of the Weight Percent of Cu_2Se NWs. The weight percent of Cu_2Se NWs in NW-n (W_n) was calculated by

$$W_n = \frac{M_{Cu}N_{Cu} + M_{Se}N_{Se}}{M_{Cu}N_{Cu} + M_{Se}N_{Se} + M_{Pedot}N_S} \times 100$$

where N_{Cu}, N_{Se}, and N_S are the amounts of Cu, Se, and S atoms in the thin films quantitatively analyzed by EDX, respectively; M_{Cu} and M_{Se} are the atomic weights of Cu and Se, respectively; M_{Pedot} is the average formula weight of PEDOT:PSS per one S atom and was estimated as 161 considering the weight ratio of PEDOT and PSS (1:1.2).

Evaluation of Thermoelectric Properties. Electrical conductivity σ was calculated from the sheet resistance measured by the van der Pauw method and the thickness measured by cross-sectional SEM images using the cutoff sample. The Seebeck coefficient S (=$\Delta V/\Delta T$) was calculated from the voltage difference (ΔV) and temperature difference (ΔT) measured by a handmade system, which was calibrated with a ZEM-3 (ADVANCE RIKO), as shown in Figure S1. For calibration of S, a 5.0 vol % PEDOT:PSS/DMSO thin film was also prepared by spin coating (1500 rpm, 45 s) and annealing (180 °C, 20 min). It is considered that the difference between the measured values by the handmade system and the ZEM-3 is due to the difference in the S values of thermocouples. These thermoelectric properties were measured at RT.

RESULTS AND DISCUSSION

Figure 2a shows the powder XRD pattern for the obtained Cu_2Se NWs. The distinct peaks indicated by rhombic marks (◆) were found to be assigned to monoclinic α-Cu_2Se. Since the observed pattern was entirely different from that for as-prepared Se NW precipitates assigned to a hexagonal Se (Figure S2a), Se NWs were considered to be completely reacted with Cu^{2+} ions. No peaks originating from metallic Cu

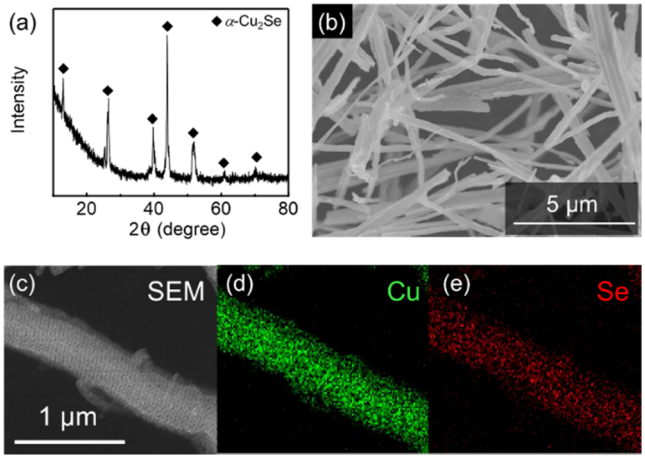

Figure 2. (a) Powder XRD pattern of Cu_2Se NWs. (b) SEM image of Cu_2Se NWs. (c−e) SEM−EDX images of Cu_2Se NWs. (c) High-magnification SEM image, and elemental mapping images of (d) Cu and (e) Se.

https://doi.org/10.1021/acsomega.2c03335
ACS Omega 2022, 7, 32101−32107

at 43.3°, Cu_2O at 36.4°, or CuO at 35.5° were observed (JCPDS file no. 5-0667 and 48-1548). No peak originating from β-Cu_2Se at 44.7° was also observed; β-Cu_2Se is not the preferable phase for thermoelectric materials because it has a higher carrier concentration than α-Cu_2Se, leading to a low Seebeck coefficient at *RT*.[45] The XRD patterns of α-Cu_2Se were maintained for 2 weeks after synthesis, indicating that the α-phase was stable at *RT* (Figure S3). Figure 2b shows the SEM image for the obtained α-Cu_2Se. As with Se NWs (Figure S2b), the one-dimensional nanostructures were observed and the diameter and length of the NWs were 300 ± 100 nm and 10 ± 5 μm, respectively. Since these values were almost the same as those of the Se NWs, it is considered that α-Cu_2Se was formed directly on the Se NWs by photoreduction. This is confirmed more clearly by elemental map images of EDX shown in Figure 2c–e. Cu species are found to be distributed along Se species on NWs. In addition, the composition ratio of Cu and Se was estimated to be 2.0:1 by the quantitative analysis of EDX and was almost the same as the stoichiometric ratio of Cu_2Se. These results indicate that single-phase α-Cu_2Se was formed by the present method.

Figure 3a shows the cross-sectional SEM image of PEDOT:PSS thin films containing Cu_2Se NWs abbreviated as NW-8. The pattern changes drastically on the upper and lower sides of the straight line indicated by the arrow. Considering that the pattern at the lower side looks monotonic, the lower side is a glass substrate. Contrary, the upper side looking complicated is a thin film. The thickness of the thin film was regarded as that of the upper side and was estimated to be ~600 nm. The thicknesses for NW-*n* are shown in Figure S4 as a function of the number of NW layers, and their values are listed in Table S1. The thickness is found to be almost proportional to the number of NW layers. This dependence indicates that the amount of deposited NWs by the spin-coating process was constant in each layer. In addition, the amount of thickness increase was less than 400 nm in the present preparation range. Considering that the average diameter of NWs was 300 nm, the NWs were planarly located in the thin film even though the spin-coating process was repeated.

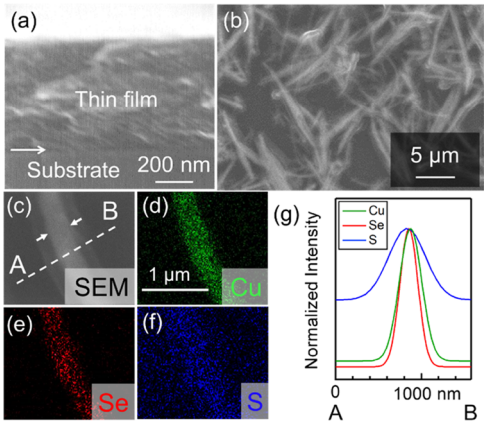

Figure 3. (a) Cross-sectional and (b) surface SEM images of NW-8. The inset in (a) is a photo image of the thin film. In (a), the arrow represents the interface between the thin film and the glass substrate. (c–f) SEM–EDX images of the thin films. (c) High-magnification SEM image, and elemental mapping images of (d) Cu, (e) Se, and (f) S. These images were obtained from the surface of the thin film. In (c), the arrows represent the core part of the NW. (g) Line profiles fitted by the Gaussian function in (d–f) for line segments A–B in (c), where the profiles were normalized by each maximum peak intensity.

The surface structure of NW-8 was observed by SEM, as shown in Figure 3b. This SEM image shows that NWs with a length of 10 ± 5 μm appeared in the thin film. Considering that the size of these NWs was almost the same as that of Cu_2Se NWs observed in Figure 2b, the Cu_2Se NWs were found to be introduced into the thin film. Looking at the enlarged SEM image (Figure 3c), it seemed that core–shell-like NWs with core parts of 350 nm indicated by arrows and shell parts of 750 nm were formed. By comparing this SEM image with elemental maps shown in Figure 3d–f, it is found that Cu and Se atoms are densely distributed along the NWs, while S atoms are distributed broader than Cu and Se atoms and even also sparsely their outside. To clarify the constituent element of core–shell NWs, line profiles in Figure 3d–f were obtained for line segments A–B in Figure 3c. The raw data of line profiles (Figure S5) were fitted by the Gaussian function and the fitted profiles were normalized by each maximum peak intensity, which is shown in Figure 3g. These profiles show that the profiles of Cu and Se from Cu_2Se NWs corresponded to the core parts of NW indicated by arrows, while that of S from PEDOT:PSS corresponded to the entire NWs, indicating that the core part was Cu_2Se NWs and the shell part was PEDOT:PSS. Additionally, almost only S was detected in the PEDOT:PSS region without NWs. These results indicated that Cu_2Se NWs were covered with PEDOT:PSS.

Figure 4a shows the amount of Cu_2Se (wt %) as a function of the number of Cu_2Se NW layers. The amount of Cu_2Se increased as the number of NW layers increased, which indicates that the amount of Cu_2Se in PEDOT:PSS thin films can be controlled by the number of NW layers. While one may wonder why the trend was not linear, this can be explained by

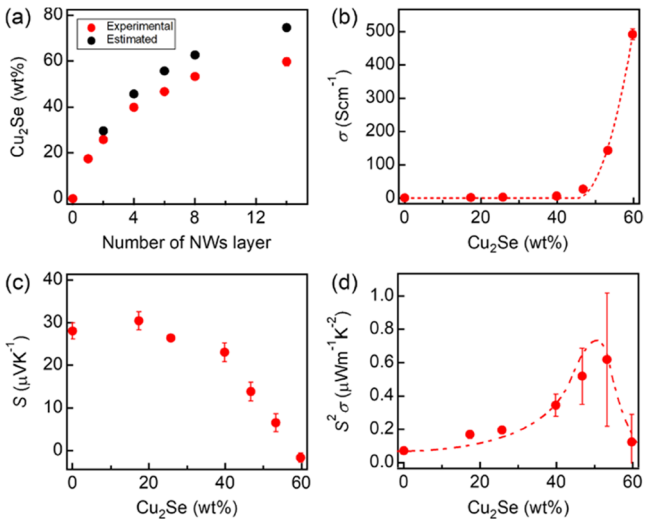

Figure 4. (a) Amount of Cu_2Se NWs (wt %) in PEDOT:PSS thin films as a function of the number of NW layers. The Cu_2Se NW amounts were quantitatively analyzed by EDX. (b) σ, (c) *S*, and (d) $S^2\sigma$ of PEDOT:PSS thin films containing Cu_2Se NWs as a function of the Cu_2Se NW amount (wt %). The sample of 0 wt % Cu_2Se NWs indicates the reference thin film of PEDOT:PSS without Cu_2Se NWs. The dashed line in (b) is the fitted curve, which is applied to experimental data with eq 2. The fitting parameters were σ_0 and W_c. The chain line in (d) is a guide to the eye.

https://doi.org/10.1021/acsomega.2c03335
ACS Omega 2022, 7, 32101–32107

the relative increase in NW layers against the static PEDOT:PSS layer. The mass ratio of NWs and the PEDOT:PSS layer is given by $\frac{n \times m_{NW}}{m_{Pedot}} = \frac{W_n}{100 - W_n}$, where m_{NW} is the mass of a single NW layer and m_{Pedot} is the mass of the PEDOT:PSS layer. Using W_1, W_n can be simply expressed as

$$W_n = \frac{W_1 \times n}{(100 - W_1) + W_1 \times n} \times 100 \quad (1)$$

The Cu_2Se amounts thus estimated are also plotted in Figure 4a. Compared with the estimated values, the experimental values were qualitatively reproduced well, although they were slightly smaller than the estimated values. This difference is probably due to the loss caused by being blown away by a part of the sample during the spin-coating process.

As shown in Figure 4b, thermoelectric properties of NW-*n* were evaluated at *RT* as a function of Cu_2Se amounts (wt %). Electrical conductivity σ of the thin films drastically increased at more than 40 wt %, while almost constant σ was obtained at less than 40 wt %. At 60 wt % corresponding to NW-14, σ was 490 S cm^{-1}, which was ~530 times larger than that of NW-0. The high σ values of the composite thin films were maintained for at least 2 weeks after synthesis (Figure S6), indicating that the thin film was stable. Considering that Cu_2Se NW films without PEDOT:PSS exhibited a higher σ of ~1200 S cm^{-1} than the PEDOT:PSS thin film (Supporting Information), this σ enhancement was due to the introduction of a high-σ material (Cu_2Se NWs). Figure S7 shows carrier concentration and hall mobility as a function of a number of NW layers obtained by Hall measurement. The carrier concentration increased by orders of magnitude as the number of NW layers increased, while the hall mobility was almost constant. This indicated that the increase of σ by the introduction of Cu_2Se NWs was due to the enhancement of the carrier concentration. The origin of the drastic increase was discussed in the next paragraph. Figure 4c shows the Seebeck coefficient *S* as a function of Cu_2Se amounts (wt %). *S* of the thin films decreases at more than 40 wt %, while *S* is almost constant at less than 40 wt %. The power factor $S^2\sigma$ of NW-8 exhibits the highest value of 0.62 μW m^{-1} K^{-2} at 53 wt %, which is ~10 times larger than that of NW-0. The effect of σ increase was larger than that of *S* decrease, although *S* decreased by the introduction of Cu_2Se NWs, leading to $S^2\sigma$ enhancement.

Here, we discuss the origin of the drastic increase of conductivity σ as observed in Figure 4b. At first, since the structural change of PEDOT:PSS by the introduction of Cu_2Se NWs can affect the conductivity, the Raman spectrum was observed, as shown in Figure S8. The peak profile of the Raman spectrum was almost the same as that of a reference film fabricated using the EtOH solution without Cu_2Se NWs instead of the EtOH dispersion of Cu_2Se NWs (NW-0-EtOH-8) including the region between 1400 and 1550 cm^{-1} due to C=C symmetric stretching vibration. The peak profile of NW-8 was also consistent with other reports.[46] This suggested that the chemical structure of PEDOT:PSS was not affected by the introduction of Cu_2Se NWs. In other words, the Cu_2Se NWs were highly probable to influence the drastic increase of σ.

As the amount of NWs increases in the thin film, the number of connections between NWs increases quadratically. The connected NWs make a conductive path, leading to the drastic increase of σ due to the so-called percolation effect. For percolation theory, σ is represented with the weight fraction *W* of fillers and the percolation threshold W_c in three-dimensional systems as follows:

$$\sigma = \begin{cases} \sigma_0(W - W_c)^2 & (W \geq W_c) \\ 0 & (W < W_c) \end{cases} \quad (2)$$

In eq 2, σ quadratically increases when *W* exceeds W_c.[47−49] We fitted the experimental data by eq 2. The fitted line (dashed line) is shown in Figure 4b, where fitting parameters W_c and σ_0 were 45 wt % and 4640 S cm^{-1}, respectively. This fitted line was in good agreement with our experimental values.

To support the value of the percolation threshold, morphological changes in the thin film were observed from surface SEM images, as shown in Figure S9a−c. For NW-1, Cu_2Se NWs form relatively small aggregates, which are isolated and distributed on the thin film without being connected to each other. In contrast, for NW-8, Cu_2Se NWs form larger aggregates, which are connected to each other everywhere. These connected Cu_2Se NWs can cause the formation of a carrier conductive path of Cu_2Se NWs, leading to a drastic increase in σ. To discuss the connection probability of NWs, the area of connected NWs was calculated by regarding them as one aggregate. Since the number of NW connections depends on the size of the aggregate, the connection probability of NWs can be discussed using the area of connected NWs. The area was calculated by ImageJ from monochrome surface images (Figure S9d−f), where the NW region was white and the other region was black. The conversion from surface SEM images to monochrome images was also done by ImageJ. The total area of Cu_2Se NWs in the range of the SEM image size was plotted as a function of the number of NW layers, as shown in Figure 5a. The total area

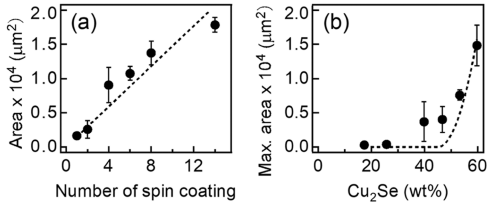

Figure 5. (a) Total area of Cu_2Se NWs in the range of 172 μm × 216 μm corresponding to the SEM image size of Figure S8 as a function of the number of NW layers. The dashed line is a linearly fitted line. (b) Maximum area (Max. area) of connected NWs as a function of Cu_2Se amounts (wt %). The area of each connected NWs was calculated by regarding them as one aggregate. Then, the maximum area in (b) is defined as the largest area in the range of the SEM image size in Figure S9. The dashed line is a fitted line by eq 3 with fitting parameter *A* and fixed parameter W_c (=45 wt %). The fitted *A* was 1.49×10^5 μm^2.

increased in proportion to the number of NW layers, where the total area was able to be linearly fitted, as shown in Figure 5a. This result indicates that the value of the area correctly represents the amount of Cu_2Se NWs in the thin film. Here, the maximum area was also extracted, which is defined as the largest area of connected Cu_2Se NWs in the range of the SEM image size, as shown in Figure S9a−c. The maximum area increases as the amount of connection increases, namely, the maximum area reflects the connection probability. Figure 5b shows that the maximum area drastically starts to increase at around 45 wt %. Since this tendency of the maximum area was

https://doi.org/10.1021/acsomega.2c03335
ACS Omega 2022, 7, 32101−32107

similar to that of σ (Figure 4b), the maximum area was fitted by the function analogous to eq 2 as follows:

$$\text{maximum area} = \begin{cases} A(W - W_c)^2 & (W \geq W_c) \\ 0 & (W < W_c) \end{cases} \quad (3)$$

where W_c is the percolation threshold used in eq 2 and A is a fitting parameter. The fitted line (dashed line) in Figure 5b reproduced the observed maximum area well. This result indicates that a percolation threshold W_c of 45 wt % obtained from σ is consistent with the structural observation. These results support the drastic increase of σ due to the percolation effect of Cu_2Se NWs.

It was previously reported that an energy barrier at the PEDOT:PSS/Cu_2Se interface was qualitatively discussed.[38] High-energy carriers can pass through the barrier, while the low-energy carrier cannot pass, which can cause the energy filtering effect, leading to S enhancement. While the σ of the composite thin films "drastically" increased (Figure 4b), S "gradually" decreased (Figure 4c). This "gradual" change can be due to the inclusion of the S enhancement effect by the energy filtering effect.

To evaluate the ZT of the composite thin films, changes in κ values were discussed qualitatively because the measurement in the in-plane direction was challenging. Since the κ of bulk Cu_2Se (1 W m^{-1} K^{-1})[50] is known to be 5 times higher than that of PEDOT:PSS (0.2 W m^{-1} K^{-1}),[51] the κ of the PEDOT:PSS/Cu_2Se NWs composite thin films is estimated to be up to 5 times higher than that of the PEDOT:PSS thin film. Even under this maximum estimation, considering the observed 10 times enhancement of $S^2\sigma$, there is still 2 times enhancement of ZT. In practice, the κ of Cu_2Se NWs is expected to be reduced from bulk Cu_2Se due to the nanostructural effect: phonon scattering at nanostructure interfaces. Therefore, the ZT of the composite thin film is more than twice as higher as that of the PEDOT:PSS thin film.

CONCLUSIONS

Cu_2Se NWs with a diameter of 300 ± 100 nm and a length of 10 ± 5 μm were synthesized by the photoreduction method. Composite thin films of Cu_2Se NWs and PEDOT:PSS were prepared by spin-coating PEDOT:PSS and Cu_2Se NWs alternatively. Conductivity σ for the composite thin films was 530 times higher than that for the PEDOT:PSS thin films. The σ of the composite thin films drastically increased at more than 40 wt % in Cu_2Se amounts, and this tendency can be quantitatively explained by the percolation effect. Consequently, the power factor $S^2\sigma$ for the composite thin films was higher than that for PEDOT:PSS thin films. This $S^2\sigma$ enhancement by the percolation effect would be expected to contribute to the development of thermoelectric performance enhancement for organic materials.

ASSOCIATED CONTENT

Supporting Information

The Supporting Information is available free of charge at https://pubs.acs.org/doi/10.1021/acsomega.2c03335.

Preparation of Cu_2Se NW films by the cold press method; hall measurement for the composite thin films; Seebeck coefficient values measured by ZEM-3 and our handmade system; XRD patterns and SEM images of Se NWs; XRD patterns of as-prepared Cu_2Se NWs and 2 weeks after synthesis; thickness of NW-n as a function of the number of Cu_2Se NW layers; line profiles in EDX images; σ of as-prepared NW-8 and 2 weeks after synthesis; carrier concentration and Hall mobility of NW-0, NW-4, and NW-8; Raman spectra of NW-8 and NW-0-EtOH-8; surface SEM images; and list of sample information (Figures S1−S9 and Table S1) (PDF)

AUTHOR INFORMATION

Corresponding Author

Hideki Tanaka − *Department of Applied Chemistry, Faculty of Science and Engineering, Chuo University, Tokyo 112-8551, Japan;* orcid.org/0000-0001-7295-1954; Email: htanaka@kc.chuo-u.ac.jp

Authors

Shunya Sakane − *Department of Applied Chemistry, Faculty of Science and Engineering, Chuo University, Tokyo 112-8551, Japan*

Shunichiro Miwa − *Department of Applied Chemistry, Faculty of Science and Engineering, Chuo University, Tokyo 112-8551, Japan*

Tatsuki Miura − *Department of Applied Chemistry, Faculty of Science and Engineering, Chuo University, Tokyo 112-8551, Japan*

Kazuki Munakata − *Department of Applied Chemistry, Faculty of Science and Engineering, Chuo University, Tokyo 112-8551, Japan*

Takafumi Ishibe − *Graduate School of Engineering Science, Osaka University, Osaka 560-8531, Japan;* orcid.org/0000-0002-8662-875X

Yoshiaki Nakamura − *Graduate School of Engineering Science, Osaka University, Osaka 560-8531, Japan*

Complete contact information is available at: https://pubs.acs.org/10.1021/acsomega.2c03335

Notes

The authors declare no competing financial interest.

ACKNOWLEDGMENTS

This work was supported by Grant-in-Aid for Early-Career Scientists Grant Number 21K14479 and Grant-in-Aid for Scientific Research (C) Grant Number 19K05187 from JSPS KAKENHI, Japan.

REFERENCES

(1) Shi, X. L.; Zou, J.; Chen, Z. G. Advanced Thermoelectric Design: From Materials and Structures to Devices. *Chem. Rev.* **2020**, *120*, 7399−7515.

(2) Tan, G.; Zhao, L. D.; Kanatzidis, M. G. Rationally Designing High-Performance Bulk Thermoelectric Materials. *Chem. Rev.* **2016**, *116*, 12123−12149.

(3) Liu, W.; Yan, X.; Chen, G.; Ren, Z. Recent Advances in Thermoelectric Nanocomposites. *Nano Energy* **2012**, *1*, 42−56.

(4) Bux, S. K.; Blair, R. G.; Gogna, P. K.; Lee, H.; Chen, G.; Dresselhaus, M. S.; Kaner, R. B.; Fleurial, J. P. Nanostructured Bulk Silicon as an Effective Thermoelectric Material. *Adv. Funct. Mater.* **2009**, *19*, 2445−2452.

(5) Hochbaum, A. I.; Chen, R.; Delgado, R. D.; Liang, W.; Garnett, E. C.; Najarian, M.; Majumdar, A.; Yang, P. Enhanced Thermoelectric Performance of Rough Silicon Nanowires. *Nature* **2008**, *451*, 163−167.

(6) Boukai, A. I.; Bunimovich, Y.; Kheli, J. T.; Yu, J. K.; Goddard, W. A.; Heath, J. R. Silicon Nanowires as Efficient Thermoelectric Materials. *Nature* **2008**, *451*, 168−171.
(7) Joshi, G.; Lee, H.; Lan, Y.; Wang, X.; Zhu, G.; Wang, D.; Gould, R. W.; Cuff, D. C.; Tang, M. Y.; Dresselhaus, M. S.; Chen, G.; Ren, Z. Enhanced Thermoelectric Figure-of-Merit in Nanostructured p-type Silicon Germanium Bulk Alloys. *Nano Lett.* **2008**, *8*, 4670−4674.
(8) Wang, X. W.; Lee, H.; Lan, Y. C.; Zhu, G. H.; Joshi, G.; Wang, D. Z.; Yang, J.; Muto, A. J.; Tang, M. Y.; Klatsky, J.; Song, S.; Dresselhaus, M. S.; Chen, G.; Ren, Z. F. Enhanced Thermoelectric Figure of Merit in Nanostructured n-type Silicon Germanium Bulk Alloy. *Appl. Phys. Lett.* **2008**, *93*, No. 193121.
(9) Biswas, K.; He, J.; Blum, I. D.; Wu, C. I.; Hogan, T. P.; Seidman, D. N.; Dravid, V. P.; Kanatzidis, M. G. High-performance Bulk Thermoelectrics with All-scale Hierarchical Architectures. *Nature* **2012**, *489*, 414−418.
(10) Nakamura, Y.; Isogawa, M.; Ueda, T.; Yamasaka, S.; Matsui, H.; Kikkawa, J.; Ikeuchi, S.; Oyake, T.; Hori, T.; Shiomi, J.; Sakai, A. Anomalous Reduction of Thermal Conductivity in Coherent Nanocrystal Architecture for Silicon Thermoelectric Material. *Nano Energy* **2015**, *12*, 845−851.
(11) Nakamura, Y. Nanostructure Design for Drastic Reduction of Thermal Conductivity While Preserving High Electrical Conductivity. *Sci. Technol. Adv. Mater.* **2018**, *19*, 31−43.
(12) Zianni, X.; Narducci, D. Synergy between Defects, Charge Neutrality and Energy Filtering in Hyper-doped Nanocrystalline Materials for High Thermoelectric Efficiency. *Nanoscale* **2019**, *11*, 7667−7673.
(13) Biswas, K.; He, J.; Zhang, Q.; Wang, G.; Uher, C.; Dravid, V. P.; Kanatzidis, M. G. Strained Endotaxial Nanostructures with High Thermoelectric Figure of Merit. *Nat. Chem.* **2011**, *3*, 160−166.
(14) Schierning, G. Silicon nanostructures for thermoelectric devices: A review of the current state of the art. *Phys. Status Solidi A* **2014**, *211*, 1235−1249.
(15) Zebarjadi, M.; Joshi, G.; Zhu, G.; Yu, B.; Minnich, A.; Lan, Y.; Wang, X.; Dresselhaus, M.; Ren, Z.; Chen, G. Power Factor Enhancement by Modulation Doping in Bulk Nanocomposites. *Nano Lett.* **2011**, *11*, 2225−2230.
(16) Yamasaka, S.; Nakamura, Y.; Ueda, T.; Takeuchi, S.; Sakai, A. Phonon Transport Control by Nanoarchitecture Including Epitaxial Ge Nanodots for Si-based Thermoelectric Materials. *Sci. Rep.* **2015**, *5*, No. 14490.
(17) Anufriev, R.; Ramiere, A.; Maire, J.; Nomura, M. Heat Guiding and Focusing Using Ballistic Phonon Transport in Phononic Nanostructures. *Nat. Commun.* **2017**, *8*, No. 15505.
(18) Sakane, S.; Ishibe, T.; Mizuta, K.; Kashino, M.; Watanabe, K.; Fujita, T.; Kamakura, Y.; Mori, N.; Nakamura, Y. Methodology of Thermoelectric Power Factor Enhancement by Nanoscale Thermal Management in Bulk SiGe Composites. *ACS Appl. Energy Mater.* **2020**, *3*, 1235−1241.
(19) Sakane, S.; Ishibe, T.; Mizuta, K.; Fujita, T.; Kiyofuji, Y.; Ohe, J.; Kobayashi, E.; Nakamura, Y. Anomalous Enhancement of Thermoelectric Power Factor by Thermal Management with Resonant Level Effect. *J. Mater. Chem. A* **2021**, *9*, 4851−4857.
(20) Vashaee, D.; Shakouri, A. Improved Thermoelectric Power Factor in Metal-Based Superlattices. *Phys. Rev. Lett.* **2004**, *92*, No. 106103.
(21) Ishibe, T.; Tomeda, A.; Watanabe, K.; Kamakura, Y.; Mori, N.; Naruse, N.; Mera, Y.; Yamashita, Y.; Nakamura, Y. Methodology of Thermoelectric Power Factor Enhancement by Controlling Nanowire Interface. *ACS Appl. Mater. Interfaces* **2018**, *10*, 37709−37716.
(22) Sakane, S.; Ishibe, T.; Taniguchi, T.; Naruse, N.; Mera, Y.; Fujita, T.; Alam, M. M.; Sawano, K.; Mori, N.; Nakamura, Y. Thermoelectric Power Factor Enhancement Based on Carrier Transport Physics in Ultimately Phonon-Controlled Si Nanostructures. *Mater. Today Energy* **2019**, *13*, 56−63.
(23) Wang, X.; Liu, P.; Jiang, Q.; Zhou, W.; Xu, J.; Liu, J.; Jia, Y.; Duan, X.; Liu, Y.; Du, Y.; Jiang, F. Efficient DMSO-Vapor Annealing for Enhancing Thermoelectric Performance of PEDOT:PSS-Based Aerogel. *ACS Appl. Mater. Interfaces* **2019**, *11*, 2408−2417.
(24) See, K. C.; Feser, J. P.; Chen, C. E.; Majumdar, A.; Urban, J. J.; Segalman, R. A. Water-Processable Polymer-Nanocrystal Hybrids for Thermoelectrics. *Nano Lett.* **2010**, *10*, 4664−4667.
(25) Ju, H.; Kim, J. Chemically Exfoliated SnSe Nanosheets and Their SnSe/Poly(3,4-ethylenedioxythiophene):Poly-(styrenesulfonate) Composite Films for Polymer Based Thermoelectric Applications. *ACS Nano* **2016**, *10*, 5730−5739.
(26) Yee, S. K.; Coates, N. E.; Majumdar, A.; Urban, J. J.; Segalman, R. A. Thermoelectric Power Factor Optimization in PEDOT:PSS Tellurium Nanowire Hybrid Composites. *Phys. Chem. Chem. Phys.* **2013**, *15*, 4024−4032.
(27) Chatterjee, K.; Mitra, M.; Kargupta, K.; Ganguly, S.; Banerjee, D. Synthesis, Characterization and Enhanced Thermoelectric Performance of Structurally Ordered Cable-like Novel Polyaniline−Bismuth Telluride Nanocomposite. *Nanotechnology* **2013**, *24*, No. 215703.
(28) Toshima, N.; Ichikawa, S. Conducting Polymers and Their Hybrids as Organic Thermoelectric Materials. *J. Electron. Mater.* **2015**, *44*, 384−390.
(29) Toshima, N.; Jiravanichanun, N.; Marutani, H. Organic Thermoelectric Materials Composed of Conducting Polymers and Metal Nanoparticles. *J. Electron Mater.* **2012**, *41*, 1735−1742.
(30) Pinter, E.; Fekete, Z. A.; Berkesi, O.; Makra, P.; Patzko, A.; Visy, C. Characterization of Poly(3-octylthiophene)/Silver Nanocomposites Prepared by Solution Doping. *J. Phys. Chem. C* **2007**, *111*, 11872−11878.
(31) Zeng, Y.; Wu, D.; Cao, X. H.; Zhou, W. X.; Tang, L. M.; Chen, K. Q. Nanoscale Organic Thermoelectric Materials: Measurement, Theoretical Models, and Optimization Strategies. *Adv. Funct. Mater.* **2020**, *30*, No. 1903873.
(32) See, K. C.; Feser, J. P.; Chen, C. E.; Majumdar, A.; Urban, J. J.; Segalman, R. A. Water-Processable Polymer-Nanocrystal Hybrids for Thermoelectrics. *Nano Lett.* **2010**, *10*, 4664−4667.
(33) Lee, W.; Kang, Y. H.; Lee, J. Y.; Jang, K. S.; Cho, S. Y. Improving the Thermoelectric Power Factor of CNT/PEDOT:PSS Nanocomposite Films by Ethylene Glycol Treatment. *RSC Adv.* **2016**, *6*, 53339−53344.
(34) Tak, J. Y.; Nam, W. H.; Lee, C.; Kim, S.; Lim, Y. S.; Ko, K.; Lee, S.; Seo, W. S.; Cho, H. K.; Shim, J. H.; Park, C. H. Ultralow Lattice Thermal Conductivity and Significantly Enhanced Near-Room-Temperature Thermoelectric Figure of Merit in α-Cu_2Se through Suppressed Cu Vacancy Formation by Overstoichiometric Cu Addition. *Chem. Mater.* **2018**, *30*, 3276−3284.
(35) Kang, S. D.; Danilkin, S. A.; Aydemir, U.; Avdeev, M.; Studer, A.; Snyder, G. J. Apparent Critical Phenomena in the Superionic Phase Transition of $Cu_{2-x}Se$. *New J. Phys.* **2016**, *18*, No. 013024.
(36) Zhang, Y.; Hu, C.; Zheng, C.; Xi, Y.; Wan, B. Synthesis and Thermoelectric Property of $Cu_{2-x}Se$ Nanowires. *J. Phys. Chem. C* **2010**, *114*, 14849−14853.
(37) Liu, B.; Ning, L.; Zhao, H.; Zhang, C.; Yang, H.; Liu, S. Visible-light Photocatalysis in Cu_2Se Nanowires with Exposed {111} Facets and Charge Separation Between (111) and $(\overline{111})$ Polar Surfaces. *Phys. Chem. Chem. Phys.* **2015**, *17*, 13280−13289.
(38) Lu, Y.; Ding, Y.; Qiu, Y.; Cai, K.; Yao, Q.; Song, H.; Tong, L.; He, J.; Chen, L. Good Performance and Flexible PEDOT:PSS/Cu_2Se Nanowire Thermoelectric Composite Films. *ACS Appl. Mater. Interfaces* **2019**, *11*, 12819−12829.
(39) Deka, S.; Genovese, A.; Zhang, Y.; Miszta, K.; Bertoni, G.; Krahne, R.; Giannini, C.; Manna, L. Phosphine-Free Synthesis of p-Type Copper(I) Selenide Nanocrystals in Hot Coordinating Solvents. *J. Am. Chem. Soc.* **2010**, *132*, 8912−8914.
(40) Miyagawa, M.; Maeda, T.; Tokuda, R.; Shibusawa, A.; Aoki, T.; Okumura, K.; Tanaka, H. Precious Metal-like Oxide-Free Copper Nanoparticles: High Oxidation Resistance and Geometric Structure. *RSC Adv.* **2016**, *6*, 104560−104565.
(41) Miyagawa, M.; Shibusawa, A.; Maeda, K.; Tashiro, A.; Sugai, T.; Tanaka, H. Diameter-Controlled Cu Nanoparticles on Saponite

https://doi.org/10.1021/acsomega.2c03335
ACS Omega 2022, 7, 32101−32107

and Preparation of Film by Using Spontaneous Phase Separation. *RSC Adv.* **2017**, *7*, 41896−41902.
(42) Miyagawa, M.; Usui, M.; Imura, Y.; Kuwahara, S.; Sugai, T.; Tanaka, H. Aqueous Synthesis of Protectant-Free Copper Nanocubes by a Disproportionation Reaction of Cu2O on Synthetic Saponite. *Chem. Commun.* **2018**, *54*, 8454−8457.
(43) Miyagawa, M.; Ikeyama, Y.; Kotake, H.; Maeda, T.; Tanaka, H. Environmental-Friendly Degradation of Clay-Hybridized Cu Nanoparticles by Carboxylic Acids. *Chem. Phys. Lett.* **2020**, *753*, No. 137615.
(44) Li, Q.; Yam, V. W. W. High-yield Synthesis of Selenium Nanowires in Water at Room Temperature. *Chem. Commun.* **2006**, 1006−1008.
(45) Scimeca, M. R.; Yang, F.; Zaia, E.; Chen, N.; Zhao, P.; Gordon, M. P.; Forster, J. D.; Liu, Y. S.; Guo, J.; Urban, J. J.; Sahu, A. Rapid Stoichiometry Control in Cu_2Se Thin Films for Room-Temperature Power Factor Improvement. *ACS Appl. Energy Mater.* **2019**, *2*, 1517−1525.
(46) Nešpůrek, S.; Kubersky, P.; Polansky, R.; Trchova, M.; Sebera, J.; Sychrovsky, V. Raman Spectroscopy and DFT Calculations of PEDOT:PSS in a Dipolar Field. *Phys. Chem. Chem. Phys.* **2021**, *24*, 541−550.
(47) Ghaderi, S.; Hassan, K. T.; Han, X.; Wang, J.; Siller, L.; Olsen, S. H. Thermoelectric Characterization of Nickel-Nanowires and Nanoparticles Embedded in Silica Aerogels. *AIP Adv.* **2018**, *8*, No. 065221.
(48) Kim, J. M.; Jang, K. S.; Lee, S. J. Electrically Conductive Polystyrene Nanocomposites Incorporated with Aspect Ratio-Controlled Silver Nanowires. *J. Appl. Polym. Sci.* **2019**, *136*, No. 47927.
(49) Gao, X.; He, M.; Liu, B.; Hu, J.; Wang, Y.; Liang, Z.; Zhou, J. Topological Design of Inorganic−Organic Thermoelectric Nanocomposites Based on "Electron-Percolation Phonon-Insulator" Concept. *ACS Appl. Energy Mater.* **2018**, *1*, 2927−2933.
(50) Liu, H.; Shi, X.; Xu, F.; Zhang, L.; Zhang, W.; Chen, L.; Li, Q.; Uher, C.; Day, T.; Snyder, G. J. Copper Ion Liquid-Like Thermoelectrics. *Nat. Mater.* **2012**, *11*, 422−425.
(51) Wang, Y.; Yang, L.; Shi, X. L.; Shi, X.; Chen, L.; Dargusch, M. S.; Zou, J.; Chen, Z. G. Flexible Thermoelectric Materials and Generators: Challenges and Innovations. *Adv. Mater.* **2019**, *31*, No. 1807916.

https://doi.org/10.1021/acsomega.2c03335
ACS Omega 2022, 7, 32101−32107